Supporting Information

Roles of Oxygen Vacancies in the Bulk and Surface of CeO_2 for Toluene Catalytic Combustion

Ziang Su[a], Wenhao Yang[a], Chizhong Wang[a], Shangchao Xiong[a], Xingzhong Cao[b], Yue Peng[a], Wenzhe Si*[a], Yibin Weng[c], Ming Xue[c], and Junhua Li[a]*

[a] State Key Joint Laboratory of Environment Simulation and Pollution Control, School of Environment, Tsinghua University, Beijing 100084, China

[b] Institute of High Energy Physics, Chinese Academy of Sciences, Beijing 100049, China

[c] State Key Laboratory of Petroleum Pollution Control, CNPC Research Institute of Safety and Environmental Technology, Beijing 102206, China

***Corresponding author.**

E-mail: pengyue83@tsinghua.edu.cn (Yue Peng)

E-mail: siwenzhe521@126.com (Wenzhe Si)

Content including: 19 pages, 11 figures, and 1 table

1. Experimental Section

1.1. Details of Catalyst Synthesis

CeO_2-S were synthesized via a previously reported method with some modifications.[1] $Ce(NO_3)_3 \cdot 6H_2O$ (2.5 g) and polyvinyl pyrrolidone (K30, 1 g) were dissolved in ethylene glycol (70 mL) to form a transparent solution. Deionized water (10 mL) was added to the solution and stirred for 30 min. Subsequently, the mixture was transferred into a 100 mL Teflon-lined stainless steel autoclave and kept in an oven at 160 ℃ for 24 h.

CeO_2-R and CeO_2-C were synthesized according to a method reported in the literature.[2] NaOH (19.2 g) and $Ce(NO_3)_3 \cdot 6H_2O$ (1.736 g) were dissolved in deionized water (70 mL and 10 mL, respectively). The two solutions were mixed under vigorous stirring and stirred for another 30 min. Then, the mixture was transferred into a 100 mL Teflon-lined stainless steel autoclave and kept in an oven at 100 ℃ and 180 ℃ for 24 h to obtain CeO_2-R and CeO_2-C samples, respectively.

After cooling to room temperature, the products obtained in the above steps were collected by centrifugation and washed with deionized water and ethanol several times. Then the products were dried at 80 ℃ for 12 h and calcinated at 500 ℃ for 3 h in static air with the heating rate of 2 ℃/min.

1.2. Details of Catalyst Characterizations

For Ce $M_{4,5}$-edge EELS spectra, all spectra were corrected by the zero-loss peak, and the background was subtracted using the power-law model. The Fourier-ratio deconvolution was also applied to eliminate the influence of sample thickness. The

white-line ratios of Ce $M_{4,5}$-edge were also calculated based on the second derivative method to quantitatively determine the Ce^{3+} concentration because the M_5/M_4 ratio increases linearly as the proportion of Ce^{3+} rises.[3, 4] The reference values of M_5/M_4 ratio for pure Ce^{3+} (1.3) and Ce^{4+} (0.9) were obtained from the literature.[3, 5]

For Ce L_3-edge XAS spectra, the radiation was monochromatized by a Si (111) double-crystal monochromator. EXAFS analysis was processed via the Athena software.[6]

For PALS spectra, a 13 μCi ^{22}Na positron source was sandwiched between two pieces of sample flakes. Total counts of 2×10^6 were acquired for all spectra to ensure accuracy. The obtained spectra were fitted by Lifetime 9.0 software and decomposed into three lifetime components. PALS is an effective technique to investigate the size, location, and relative concentration of oxygen vacancies in CeO_2-based catalysts.[7] In general, the electron density at the annihilation site has a great influence on the positron lifetime, and the lifetime increases with the decrease of electron density.[8]

For O_2-TPD experiments, all samples were pretreated under inert gas at 300 ℃ for 1h. After cooling to 50 ℃, the gas flow was changed to 50 mL·min^{-1} of 5% O_2/He and maintained for 1 h. After that, the samples were purged with He flow for 1h and then heated from 50 ℃ to 1000 ℃ at the rate of 10℃·min^{-1}. For H_2-TPR experiments, all samples were pretreated under Ar flow at 300 ℃ for 1h. After cooling to room temperature, the gas flow was changed to 50 mL·min^{-1} of 5% H_2/Ar and maintained for 1 h. After that, the samples were heated to 1000 ℃ at the rate of 10℃·min^{-1}. The

formed water vapor was removed by a cooler. Signals were recorded by a TCD detector.

For Toluene-TPD experiments, all samples were treated in the reaction atmosphere (1000 ppm toluene + 21% O_2 + 79% N_2, 100 mL·min^{-1}) at 50 ℃ to adsorb toluene. After catalyst adsorption is saturated, the gas flow was changed to 100 mL·min^{-1} of N_2. The samples were firstly purged with N_2 for 1h and then heated from 50 ℃ to 800 ℃ at the rate of 10℃·min^{-1}. The concentrations of toluene, CO, and CO_2 were recorded by the FTIR detector.

For In-situ DRIFTS, all samples were purged with air at 300 ℃ for 1 h to remove impurities adsorbed on the surface. After pretreatment, toluene (300 ppm toluene + 21%O_2 + 79% N_2) was introduced to the reaction cell at 30 ℃ and maintained for 1 h. Thereafter, the temperature was gradually raised to 250 ℃ and kept at each sampling temperature for 15 min before the spectra collection.

1.3. Details of Catalytic Performance Evaluation and Stability Test

Surface Ce^{3+} sites normalized reaction rates (r_{Ce3+}, s^{-1}) and S_{BET} normalized reaction rates (r_S, mol·m^{-2}·s^{-1}) were calculated by the following formula

$$r_{Ce^{3+}}\left(s^{-1}\right) = -\frac{C_{inlet} \bullet F}{m_{cat} \bullet S_{BET} \bullet [Ce^{3+}_{sur}] \bullet \rho} \bullet \ln(1 - X_{toluene}) \quad (1)$$

$$r_S\left(mol \bullet m^{-2} \bullet s^{-1}\right) = -\frac{C_{inlet} \bullet F}{m_{cat} \bullet S_{BET}} \bullet \ln(1 - X_{toluene}) \quad (2)$$

where C_{inlet} refer to the toluene concentration in the inlet gas, F (mol·s^{-1}) is the flow rate, m_{cat} (g) is the mass of catalyst, S_{BET} (m^2·g^{-1}) is the specific surface area calculated via BET method, [Ce^{3+}_{sur}] (%) is the surface Ce^{3+} proportion derived from

Ce 3d XPS spectra (Figure S1, Table 1), ρ (mol·m^{-2}) is the density of surface Ce atoms calculated by CeO_2 surface models (Figure S2).

The 100 h stability test of CeO_2-S was conducted on the same device as catalytic performance evaluation. 100 mg of CeO_2-S (40−60 mesh) was treated in the reaction atmosphere (1000 ppm toluene + 21% O_2 + 79% N_2, 100 mL·min^{-1}), and the temperature was maintained at 220 ℃ for 100 h.

1.4. Details of DFT+U Calculation

First-principles calculations based on density functional theory (DFT) were carried out with the Vienna Ab-initio simulation package (VASP) and PW91 functional. [9, 10] The interaction between core electrons and valence electrons was expressed by the projector-augmented wave (PAW) method.[11] The cutoff energy of the plane-wave basis set was set to 400 eV. To guarantee the accuracy, the convergence criteria of energy and force were set to 10^{-6} eV and 0.02 eV·Å^{-1}, respectively. DFT+U with U = 5 eV was applied to treat Ce 4f orbital.[12, 13]

To simulate CeO_2 samples, three slab models were constructed with a vacuum region of 15 Å. For CeO_2-S with a step-like structure, a 3 × 2 (331) slab model was employed.[12] For CeO_2-R, a 3 × 3 (110) slab model was used. For CeO_2-C, a 3 × 3 (100) slab model was built, and half of the top oxygen atoms were moved to the bottom for simulation of surface reconstruction.[13, 14] Before calculation, no more than half of the atomic layers from the bottom were fixed. The Brillouin zone of (331) model was sampled using a Monkhorst–Pack k-point set of 2 × 1 × 1, whereas those of other two models were sampled by a 2 × 2 × 1 k-point set to acquire similar sampling densities.

109

2. Supporting Figures

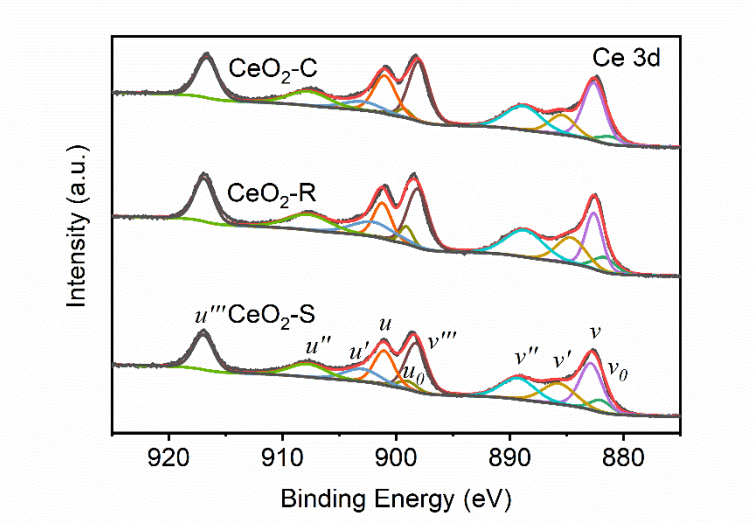

Figure S1. Ce 3d XPS spectra of CeO_2 samples.

All spectra were deconvoluted into ten components. Specifically, the peaks of $3_{d5/2}$ include v_0, v, v', v'', and v''', and the peaks of $3d_{3/2}$ consist of u_0, u, u', u'', and u'''.[15, 16] Among the components, the spin-orbit split doublets including v, v'', v''', u, u'', and u''' arise from the 4f configuration of Ce^{4+}, and the other four peaks indicate the presence of Ce^{3+}.[17] After the deconvolution, the proportions of surface Ce^{3+} ($[Ce^{3+}_{sur}]$) were calculated by the equation

$$[Ce^{3+}_{sur}] = \frac{v_0 + v' + u_0 + u'}{v_0 + v + v' + v'' + v''' + u_0 + u + u' + u'' + u'''} \quad (3)$$

where v_0, v, v', v'', v''', u_0, u, u', u'', and u''' refers to the integrated intensities of corresponding peaks. The $[Ce^{3+}_{sur}]$ values are shown in Table 1.

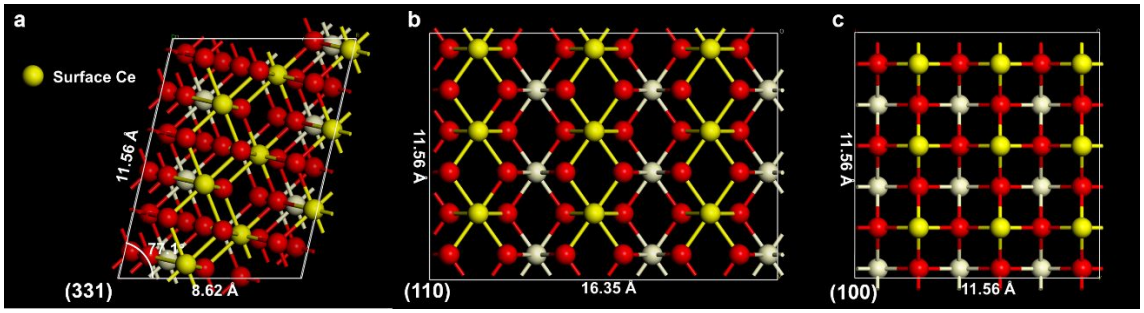

Figure S2. Top views of CeO_2 surface structures. (**a**) (331) plane for CeO_2-S, (**b**) (110) plane for CeO_2-R, (**c**) (100) plane for CeO_2-C.

3×3 supercell surface structures of CeO_2 (110) and (100) planes were built to calculate the surface Ce atom concentrations (ρ, $mol \cdot m^{-2}$) of CeO_2-R and CeO_2-C. According to the previously reported literature, (331) plane was chosen for CeO_2-S to simulate the (111) planes with step-like structures.[12]

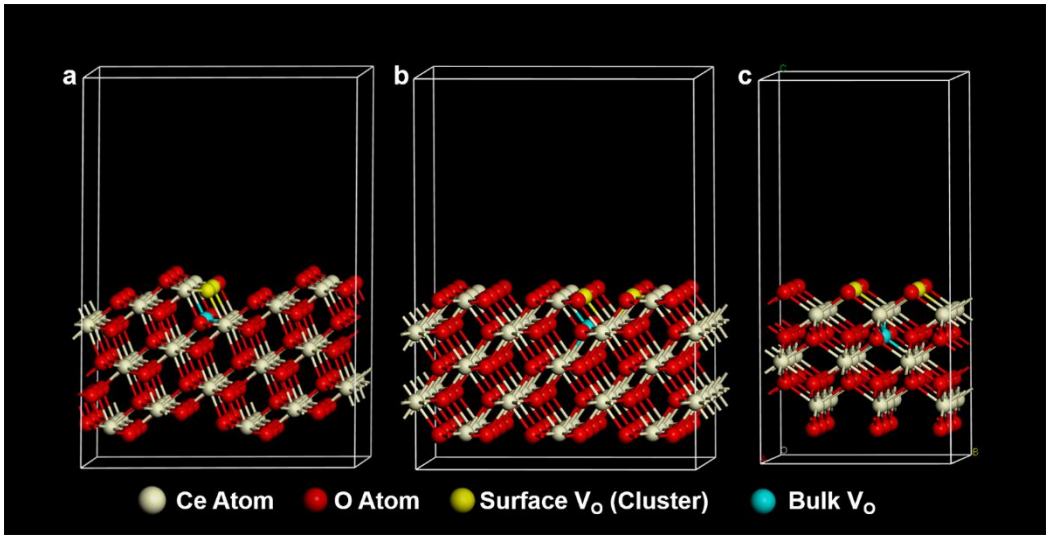

Figure S3. CeO_2 slab models for DFT+U calculation. (**a**) (331) slab model for CeO_2-S, (**b**) (110) slab model for CeO_2-R, (**c**) (100) slab model for CeO_2-C. The white, red, yellow, and blue atoms refer to Ce atom, O atom, surface oxygen vacancy (clusters), and bulk oxygen vacancy, respectively.

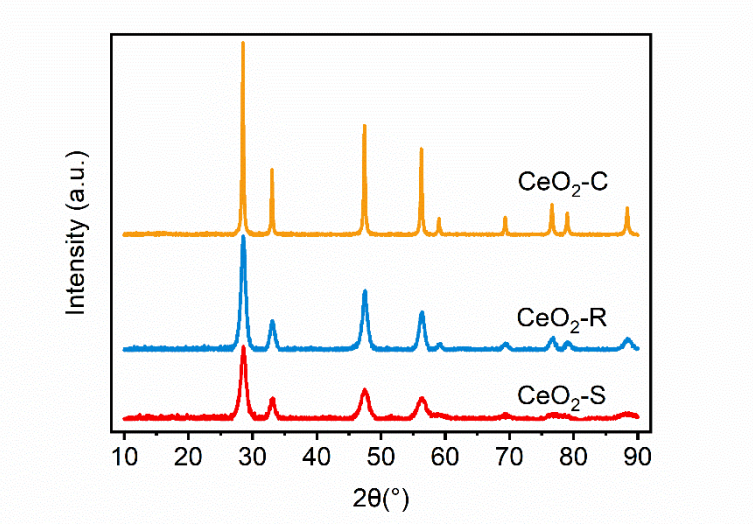

139

140 **Figure S4.** XRD patterns of CeO_2 samples.

141

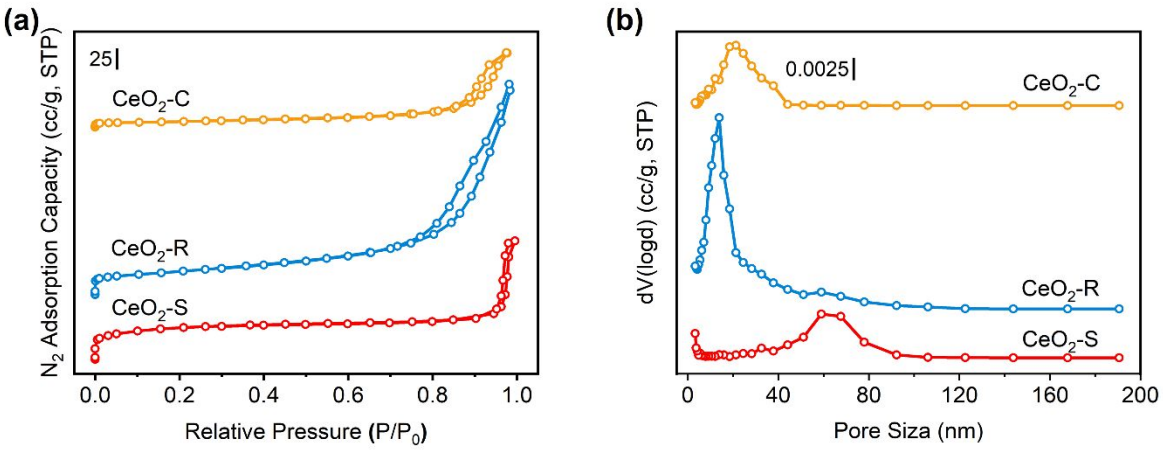

142

143 **Figure S5.** (a) N_2 adsorption-desorption isotherms and (b) BJH pore size distributions

144 of nanoceria catalysts.

145

146

147

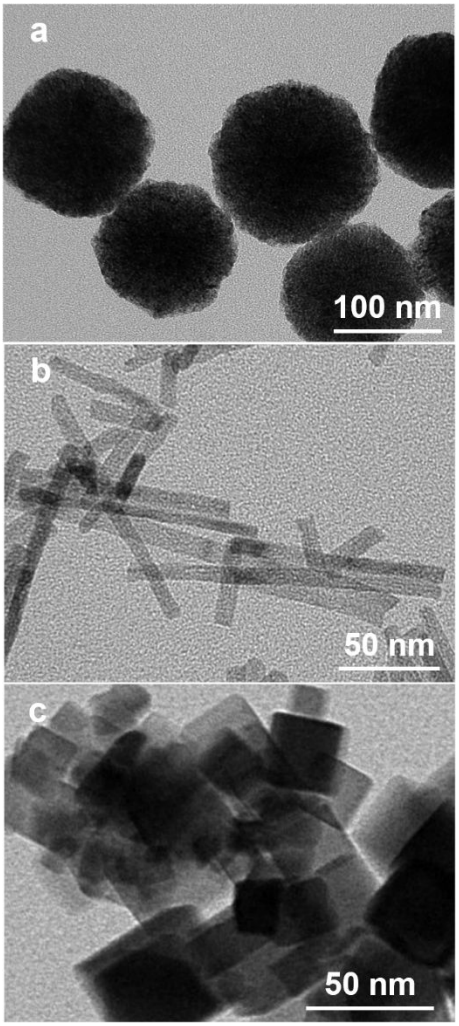

Figure S6. Low-magnification TEM images of CeO_2 samples. (**a**) CeO_2-S, (**b**) CeO_2-R, (**c**) CeO_2-C.

153 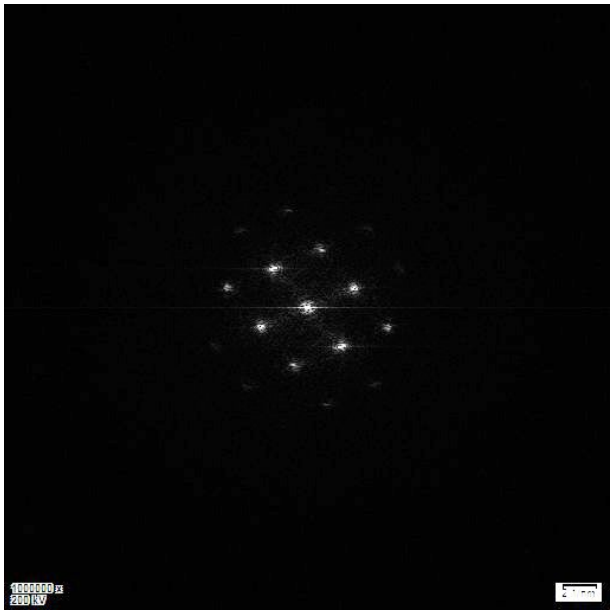

154 **Figure S7.** SAED images of CeO_2-S.

155

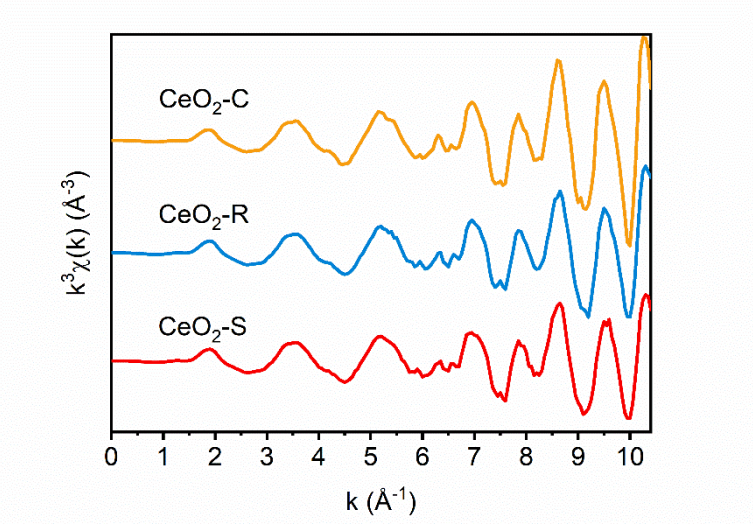

156

157 **Figure S8.** k^2-weighted Ce L_3-edge EXAFS spectra of CeO_2 samples.

158

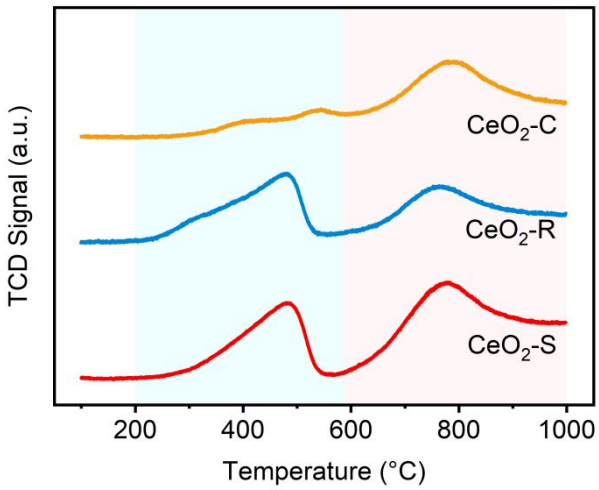

Figure S9. H_2-TPR profile of CeO_2 samples.

The peak at a lower temperature (200−600 ℃) is attributed to the reduction of Ce^{4+} on the top layers of CeO_2 particle: the main peak at ~ 480 ℃ arises from the active lattice oxygen, whereas the shoulder peak at ~ 300 ℃ is due to the adsorbed oxygen species. [18, 19] Consistent with O_2-TPD, CeO_2-R exhibits the highest amount of adsorbed oxygen. However, much more lattice oxygen of CeO_2-S was reducted than CeO_2-R and CeO_2-C, endowing this sample with excellent redox property and catalytic combustion activity.

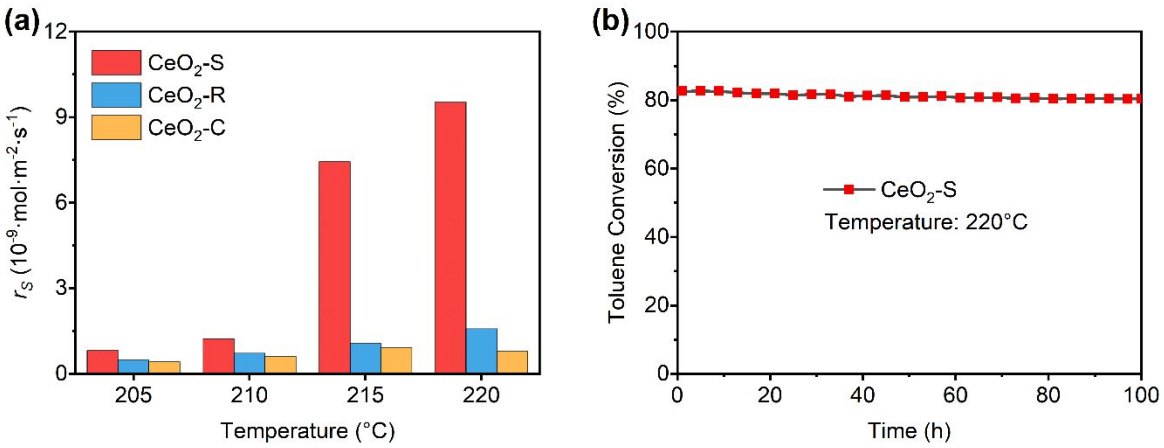

169

170 **Figure S10.** (**a**) S_{BET} normalized reaction rates of CeO_2 samples for toluene catalytic

171 combustion, (**b**) stability test profile of CeO_2-S.

172

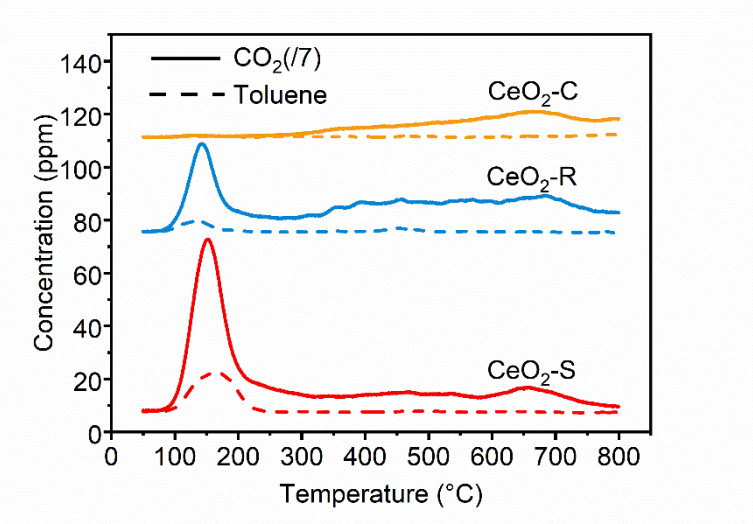

173

174 **Figure S11.** Toluene-TPD profile of CeO_2 samples.

175

3. Supporting Table

Table S1. Assignment of the in-situ DRIFTS bands for toluene adsorption and catalytic combustion.

Wavenumber (cm^{-1})	Vibration	Species
3000-3500 (br)	σ(O–H) (Polymerized) [a]	Water [20]
2966 (s)	σ(C–H) [a]	Aromatic ring [21]
2940 (m), 2860 (s)	σ(C–H) [a]	Methyl group [22]
2917 (m), 2820 (m)	σ(C–H) [a]	Methylene group [22]
1918 (w)	σ(C=O) [a]	Maleic anhydride [23, 24]
1650 (s)	σ(C=O) [a]	Aldehyde group [25]
1635 (w)	δ(H–O–H) [b]	Water [20]
1589 (vs), 1530 (vs), 1295 (s)	σ($-COO^-$) [a]	Carboxylate [c] [21, 26]
1573 (vs), 1525 (vs)	σ($-COO^-$) [a]	Bidentate carbonate [27]
1560 (s), 1500 (m)	σ(C=C) [a]	Aromatic ring [26]
1430 (vs)	δ(C–H) [b]	Methylene group [28]
1380 (s)	δ(C–H) [b]	Methyl group [28]
1112 (vs), 1062 (vs), 1040 (vs)	σ(C–O) [a]	Phenolate [29]
937 (w)	δ(C=C) [b]	Maleic anhydride [23, 24]
906 (s), 888 (s), 855 (s)	δ(C–H) [b]	Aromatic ring [26]

[a] σ refers to stretching vibration.

[b] δ refers to bending vibration.

[c] Carboxylate species refer to benzoate at low temperatures and chain carboxylate at high temperatures.

References:

1. Liu, W.; Liu, X.; Feng, L.; Guo, J.; Xie, A.; Wang, S.; Zhang, J.; Yang, Y., The synthesis of CeO_2 nanospheres with different hollowness and size induced by copper doping. *Nanoscale* **2014,** *6*, (18), 10693-700.

2. Mai, H. X.; Sun, L. D.; Zhang, Y. W.; Si, R.; Feng, W.; Zhang, H. P.; Liu, H. C.; Yan, C. H., Shape-selective synthesis and oxygen storage behavior of ceria nanopolyhedra, nanorods, and nanocubes. *J. Phys. Chem. B* **2005,** *109*, (51), 24380-24385.

3. Yang, G.; Mobus, G.; Hand, R. J., Cerium and boron chemistry in doped borosilicate glasses examined by EELS. *Micron* **2006,** *37*, (5), 433-441.

4. Spadaro, M. C.; Luches, P.; Bertoni, G.; Grillo, V.; Turner, S.; Van Tendeloo, G.; Valeri, S.; D'Addato, S., Influence of defect distribution on the reducibility of CeO_{2-x} nanoparticles. *Nanotechnology* **2016,** *27*, (42).

5. Lavkova, J.; Khalakhan, I.; Chundak, M.; Vorokhta, M.; Potin, V.; Matolin, V.; Matolinova, I., Growth and composition of nanostructured and nanoporous cerium oxide thin films on a graphite foil. *Nanoscale* **2015,** *7*, (9), 4038-4047.

6. Ravel, B.; Newville, M., ATHENA, ARTEMIS, HEPHAESTUS: data analysis for X-ray absorption spectroscopy using IFEFFIT. *J. Synchrotron Radiat.* **2005,** *12*, (4), 537-541.

7. Kong, M.; Li, Y.; Chen, X.; Tian, T.; Fang, P.; Zheng, F.; Zhao, X., Tuning the relative concentration ratio of bulk defects to surface defects in TiO_2 nanocrystals leads to high photocatalytic efficiency. *J. Am. Chem. Soc.* **2011,** *133*, (41), 16414-

16417.

8. Guan, M.; Xiao, C.; Zhang, J.; Fan, S.; An, R.; Cheng, Q.; Xie, J.; Zhou, M.; Ye, B.; Xie, Y., Vacancy associates promoting solar-driven photocatalytic activity of ultrathin bismuth oxychloride nanosheets. *J. Am. Chem. Soc.* **2013,** *135*, (28), 10411-7.

9. Kresse, G.; Furthmuller, J., Efficiency of ab-initio total energy calculations for metals and semiconductors using a plane-wave basis set. *Comp. Mater. Sci.* **1996,** *6*, (1), 15-50.

10. Perdew, J. P.; Wang, Y., Accurate and simple analytic representation of the electron-gas correlation-energy. *Phys. Rev. B* **1992,** *45*, (23), 13244-13249.

11. Blochl, P. E., Progector Augmented-Wave Method. *Phys. Rev. B* **1994,** *50*, (24), 17953-17979.

12. Liu, J. C.; Wang, Y. G.; Li, J., Toward rational design of oxide-supported single-atom catalysts: Atomic dispersion of gold on ceria. *J. Am. Chem. Soc.* **2017,** *139*, (17), 6190-6199.

13. Wang, J.; Tan, H. Y.; Yu, S. Z.; Zhou, K. B., Morphological effects of gold clusters on the reactivity of ceria surface oxygen. *ACS Catal.* **2015,** *5*, (5), 2873-2881.

14. Nolan, M., Hybrid density functional theory description of oxygen vacancies in the CeO_2 (110) and (100) surfaces. *Chem. Phys. Lett.* **2010,** *499*, (1-3), 126-130.

15. Hu, Z.; Liu, X.; Meng, D.; Guo, Y.; Guo, Y.; Lu, G., Effect of ceria crystal plane on the physicochemical and catalytic properties of Pd/ceria for CO and propane oxidation. *ACS Catal.* **2016,** *6*, (4), 2265-2279.

16. Rodriguez, J. A.; Ma, S.; Liu, P.; Hrbek, J.; Evans, J.; Perez, M., Activity of CeO_x

231 and TiO_x nanoparticles grown on Au(111) in the water-gas shift reaction. *Science* **2007,**
232 *318*, (5857), 1757-1760.
233 17. Yang, F.; Graciani, J.; Evans, J.; Liu, P.; Hrbek, J.; Sanz, J. F.; Rodriguez, J. A.,
234 CO oxidation on inverse CeO_x/Cu(111) catalysts: high catalytic activity and ceria-
235 promoted dissociation of O_2. *J. Am. Chem. Soc.* **2011,** *133*, (10), 3444-51.
236 18. Huang, H.; Dai, Q. G.; Wang, X. Y., Morphology effect of Ru/CeO_2 catalysts for
237 the catalytic combustion of chlorobenzene. *Appl. Catal. B-Environ.* **2014,** *158*, 96-105.
238 19. Afzal, S.; Quan, X.; Lu, S., Catalytic performance and an insight into the
239 mechanism of CeO_2 nanocrystals with different exposed facets in catalytic ozonation
240 of p-nitrophenol. *Appl. Catal. B-Environ.* **2019,** *248*, 526-537.
241 20. Qu, Z.; Bu, Y.; Qin, Y.; Wang, Y.; Fu, Q., The effects of alkali metal on structure of
242 manganese oxide supported on SBA-15 for application in the toluene catalytic
243 oxidation. *Chem. Eng. J.* **2012,** *209*, 163-169.
244 21. Zhao, S.; Hu, F.; Li, J., Hierarchical core-shell Al_2O_3@Pd-CoAlO microspheres for
245 low-temperature toluene combustion. *ACS Catal.* **2016,** *6*, (6), 3433-3441.
246 22. Wang, M.; Zhang, F.; Zhu, X.; Qi, Z.; Hong, B.; Ding, J.; Bao, J.; Sun, S.; Gao, C.,
247 DRIFTS evidence for facet-dependent adsorption of gaseous toluene on TiO_2 with
248 relative photocatalytic properties. *Langmuir* **2015,** *31*, (5), 1730-1736.
249 23. Santos, V. P.; Pereira, M. F. R.; Orfao, J. J. M.; Figueiredo, J. L., The role of lattice
250 oxygen on the activity of manganese oxides towards the oxidation of volatile organic
251 compounds. *Appl. Catal. B-Environ.* **2010,** *99*, (1-2), 353-363.
252 24. Yang, L.; Zhang, F.; Endo, T.; Hirotsu, T., Microstructure of maleic anhydride

253 grafted polyethylene by high-resolution solution-state NMR and FTIR spectroscopy.
254 *Macromolecules* **2003,** *36*, (13), 4709-4718.
255 25. Hou, Z.; Zhou, X.; Lin, T.; Chen, Y.; Lai, X.; Feng, J.; Sun, M., The promotion effect
256 of tungsten on monolith Pt/$Ce_{0.65}Zr_{0.35}O_2$ catalysts for the catalytic oxidation of toluene.
257 *New J. Chem.* **2019,** *43*, (15), 5719-5726.
258 26. Zhao, L.; Zhang, Z.; Li, Y.; Leng, X.; Zhang, T.; Yuan, F.; Niu, X.; Zhu, Y.,
259 Synthesis of Ce_aMnO_x hollow microsphere with hierarchical structure and its excellent
260 catalytic performance for toluene combustion. *Appl. Catal. B-Environ.* **2019,** *245*, 502-
261 512.
262 27. Chen, X.; Cai, S.; Yu, E.; Chen, J.; Jia, H., MnO_x/Cr_2O_3 composites prepared by
263 pyrolysis of Cr-MOF precursors containing in situ assembly of MnO_x as high stable
264 catalyst for toluene oxidation. *Appl. Surf. Sci.* **2019,** *475*, 312-324.
265 28. Busca, G., Infrared studies of the reactive adsorption of organic molecules over
266 metal oxides and of the mechanisms of their heterogeneously-catalyzed oxidation.
267 *Catal. Today* **1996,** *27*, (3-4), 457-496.
268 29. Rainone, F.; Bulushev, D. A.; Kiwi-Minsker, L.; Renken, A., DRIFTS and transient-
269 response study of vanadia/titania catalysts during toluene partial oxidation. *Phys.*
270 *Chem. Chem. Phys.* **2003,** *5*, (20), 4445-4449.
271